

## Simulation of Turbulent Flows Using a Finite-Volume Based Lattice Boltzmann Flow Solver

Goktan Guzel\* and Ilteris Koc

*ASELSAN Inc, MGEO Division, Etlik 06011, Ankara, TURKEY.*

Received 4 March 2014; Accepted (in revised version) 1 August 2014

Communicated by Kazuo Aoki

---

**Abstract.** In this study, the Lattice Boltzmann Method (LBM) is implemented through a finite-volume approach to perform 2-D, incompressible, and turbulent fluid flow analyses on structured grids. Even though the approach followed in this study necessitates more computational effort compared to the standard LBM (the so called stream and collide scheme), using the finite-volume method, the known limitations of the stream and collide scheme on lattice to be uniform and Courant-Friedrichs-Lewy (CFL) number to be one are removed. Moreover, the curved boundaries in the computational domain are handled more accurately with less effort. These improvements pave the way for the possibility of solving fluid flow problems with the LBM using coarser grids that are refined only where it is necessary and the boundary layers might be resolved better.

**AMS subject classifications:** 76M12, 76M28, 76D99, 76F99

**Key words:** Lattice Boltzmann Method, finite-volume approach, turbulent flows.

---

## 1 Introduction

The LBM is a fairly new numerical method to simulate fluid flows and can be considered as an alternative to the classical Navier-Stokes (NS) equations based methods. The LBM originated from the Lattice-Gas Automata (LGA) method which can be thought as a simple Molecular Dynamics model. The purpose of the LGA method is to simulate the behavior and interaction of particles in a gas as simple as possible [1]. For this purpose, the gas is modeled as a cluster of solid spheres moving along a uniform lattice. Each solid sphere has a discrete set of possible velocities and the collision between separate particles is handled by a set of elastic collision rules. Macroscopic quantities, such as particle

---

\*Corresponding author. *Email addresses:* goguzel@aselsan.com.tr (G. Guzel), ikoc@aselsan.com.tr (I. Koc)

density and velocity at each lattice node, can be computed using the microscopic quantities, making it possible to study the macroscopic behavior of a fluid flow. Even though the idea is simple, the method still provides similar solutions as the NS equations based methods do. Beyond being simple, it has the advantage of low memory requirement. The method is also highly parallelizable because of the locality of the data access pattern. However, numerically, the LGA method suffers the statistical noise caused by the averaging procedure to obtain the macroscopic properties from the microscopic properties.

To remedy the statistical noise that the LGA method suffers, the LBM was developed. Being a derivative of the LGA method, the LBM basically relies on the same idea. But, instead of handling single particles, the LBM handles particle distributions. This removes the need for averaging to obtain the macroscopic properties from the microscopic properties, so the statistical noise is also removed. Even though the LBM is more memory intensive compared to the LGA method since it is based on particle distributions that are in floating point numbers, it retains some of the advantages that LGA method has, such as being simple and having a high degree of parallelization potential. In addition to above mentioned advantages, the solution of computationally expensive Poisson equation, which is required when using NS equations based methods, is not needed when using the LBM. Also, since no pressure-velocity coupling is needed, unlike the NS equations based methods; one does not have to use complex staggered-grid systems. Furthermore, the equations solved when using the LBM are linear, so the solution time is reduced significantly since the solution procedure does not necessitate any iterative algorithm. These properties make the LBM an attractive method, and there is an increasing interest for the LBM in the Computational Fluid Dynamics (CFD) community. As a result, the progress in developing and employing the LBM is rapid. The recent applications range from multiphase flow simulations [2] to aero-acoustic simulations [3], from high resolution turbulence simulations [4] to biological flow simulations [5].

Even though the LBM in its standard form, which basically consists of streaming and collision steps, looks very attractive as mentioned above, the method is strictly restrictive about the uniformity of the computational grid. This restriction is inherited from the LGA method in which the particles modeled have to move to the next link after a time step. This shortcoming in turn dictates that the CFL number has to be equal to one. These are the major handicaps on widespread use of LBM in engineering problems. So, a lot of research has been going on to improve these aspects of LBM. One of the first efforts toward improving standard LBM is the work of He et al. [6]. In that work, an interpolation based approach is applied at every time step to obtain the distribution function at points of a non-uniform grid. Since the interpolation procedure is very time consuming and the accuracy of the method highly depends on the interpolation scheme used, this method is not very practical comparing to the standard LBM. Another approach proposed by Filipova and Hanel [7] is based on the idea of grid refinement method. With this approach, a coarser background grid is generated and a local refinement is performed in critical regions. Even though it is less complicated, an interpolation scheme is still needed for this method to transfer data from different levels of grid. The last approach, which is also

used in this work, was first proposed by Succi et al. [8]. This approach relies on the finite-volume formulation of the Lattice Boltzmann Equation (LBE) and makes it possible to separate space and time discretization, while utilizing structured but non-uniform grids.

In this study, the LBM is implemented through a finite-volume approach to perform 2-D, incompressible, and turbulent fluid flow analyses on structured grids. Even though the approach followed in this study necessitates more computational effort over the standard LBM; using the finite-volume method, the known limitations of the stream and collide scheme on lattice to be uniform and CFL number to be one are removed. Moreover, the curved boundaries in the computational domain are handled more accurately with less effort. This improvement paves the way for the possibility of solving fluid flow problems with the LBM using coarser grids that are refined only where it is necessary and the boundary layers might be resolved better.

## 2 The numerical model

### 2.1 Discrete velocity Boltzmann equation

The starting point of the LBM is the continuous form of the Boltzmann Equation with Bhatnagar-Gross-Krook (BGK) [9] approximation for the collision operator

$$\frac{\partial f}{\partial t} + \vec{e} \cdot \vec{\nabla} f = -\frac{1}{\lambda}(f - f^{eq}), \quad (2.1)$$

where  $f = f(\vec{x}, \vec{e}, t)$  is the particle distribution function, in which  $\vec{x}$  is the position vector,  $\vec{e}$  is the particle velocity vector,  $t$  is the time,  $f^{eq}$  is the equilibrium distribution function (or Maxwell-Boltzmann distribution function), and  $\lambda$  is the relaxation time. The right hand side of Eq. (2.1) is the collision operator.

To solve  $f$  numerically, Eq. (2.1) is discretized in the velocity space using a set of velocities,  $\vec{e}_\alpha$ :

$$\frac{\partial f_\alpha}{\partial t} + \vec{e}_\alpha \cdot \vec{\nabla} f_\alpha = -\frac{1}{\lambda}(f_\alpha - f_\alpha^{eq}). \quad (2.2)$$

In Eq. (2.2),  $f_\alpha$  is the distribution function associated with the  $\alpha^{th}$  discrete velocity,  $\vec{e}_\alpha$ . For 2-D problems, one might use D2Q9 [10] model of which the discrete velocities are shown in Fig. 1.

The discrete velocities of D2Q9 model are given by

$$\begin{aligned} e_0 &= 0, \\ e_{\alpha x, \alpha y} &= c(\cos((\alpha-1)*\pi/2), \sin((\alpha-1)*\pi/2)) \quad \text{for } \alpha = 1, 2, 3, 4, \\ e_{\alpha x, \alpha y} &= \sqrt{2}c(\cos((\alpha-5)*\pi/2 + \pi/4), \sin((\alpha-5)*\pi/2 + \pi/4)) \quad \text{for } \alpha = 5, 6, 7, 8, \end{aligned} \quad (2.3)$$

where  $c$  is an arbitrary constant related to the speed of sound and is given by  $c = c_s \sqrt{3}$ .

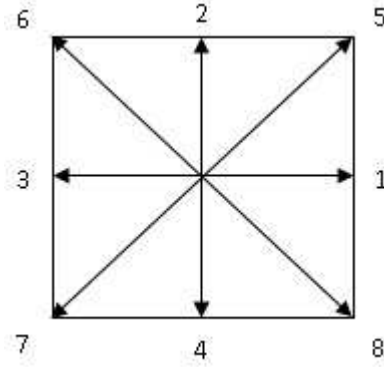


Figure 1: Discrete velocities of D2Q9 model.

The equilibrium distribution functions for D2Q9 model is given by

$$f_{\alpha}^{eq} = \rho \omega_{\alpha} \left[ 1 + 3 \frac{\vec{e}_{\alpha} \cdot \vec{u}}{c^2} + \frac{9}{2} \frac{(\vec{e}_{\alpha} \cdot \vec{u})^2}{c^4} - \frac{3}{2} \frac{(\vec{u})^2}{c^2} \right], \quad (2.4)$$

where  $\omega_{\alpha}$  is the weighting factor and equals to  $4/9$  for  $\alpha = 0$ ,  $1/9$  for  $\alpha = 1-4$ , and  $1/36$  for  $\alpha = 5-8$ .  $\rho = \sum_{\alpha} f_{\alpha}$  is the macroscopic density and  $\rho \vec{u} = \sum_{\alpha} f_{\alpha} \vec{e}_{\alpha}$  is the macroscopic momentum. Pressure is related with density through  $p = c_s^2 \rho$  and the relaxation time is a function of kinematic viscosity,  $\nu$ , that is given by  $\lambda = \nu / c_s^2$ .

## 2.2 The non-dimensional form

The non-dimensional form of the discrete velocity Boltzmann Equation might be obtained by introducing the non-dimensional variables in Table 1, where  $L$  is the characteristic length and the characteristic velocity is chosen to be  $c$ . With the introduced variables,

Table 1: Dimensional parameters and their non-dimensional forms.

	Dimensional	Non-dimensional
Length	$x$	$\hat{x} = \frac{x}{L}$
Time	$t$	$\hat{t} = \frac{tc}{L}$
Macroscopic velocity	$\vec{u}$	$\vec{\hat{u}} = \frac{\vec{u}}{c}$
Discrete velocity	$\vec{e}_{\alpha}$	$\vec{\hat{e}}_{\alpha} = \frac{\vec{e}_{\alpha}}{c}$
Distribution function	$f_{\alpha}$	$\hat{f}_{\alpha} = \frac{f_{\alpha}}{\rho_{\infty}}$
Macroscopic density	$\rho$	$\hat{\rho} = \frac{\rho}{\rho_{\infty}}$
Pressure	$p$	$\hat{p} = \frac{p}{\rho c_s^2}$
Kinematic viscosity	$\nu$	$\hat{\nu} = \frac{\nu}{cL}$

Eq. (2.2) can be rewritten in non-dimensional form as

$$\frac{\partial \hat{f}_\alpha}{\partial \hat{t}} + \hat{e}_\alpha \cdot \hat{\nabla} \hat{f}_\alpha = -\frac{1}{\lambda} (\hat{f}_\alpha - \hat{f}_\alpha^{eq}). \quad (2.5)$$

In Eq. (2.5), the non-dimensional equilibrium distribution function,  $\hat{f}_\alpha^{eq}$ , is given by

$$\hat{f}_\alpha^{eq} = \hat{\rho} \omega_\alpha \left[ 1 + 3\hat{e}_\alpha \cdot \hat{u} + \frac{9}{2} (\hat{e}_\alpha \cdot \hat{u})^2 - \frac{3}{2} \hat{u}^2 \right]. \quad (2.6)$$

It is also notable that when the kinematic viscosity is non-dimensionalized, an important relationship between the kinematic viscosity and the other flow parameters is obtained;

$$\hat{\nu} = \frac{Ma_\infty}{\sqrt{3} Re_\infty}. \quad (2.7)$$

Here,  $Re_\infty$  is the reference Reynolds number and  $Ma_\infty$  is the reference Mach number. It should also be stated now that, for the rest of the paper, the hats over the variables will be omitted for convenience of writing.

### 2.3 Finite-volume formulation of the LBM

The present implementation of the LBM is based on the well-established and generally accepted form of the finite-volume formulation that utilizes integral form of a governing equation and solves it over control volumes that cover the solution domain. The same formulation is also used in the previous works of Peng et al. [11], Stiebler et al. [12], Patil et al. [13], and Zarghami et al. [14] for the LBM. Stating first that the present implementation follows a cell-centered approach, the formulation starts with the integration of Eq. (2.5) over the control volume, quadrilateral cells in this case, that form a structured grid as shown in Fig. 2.

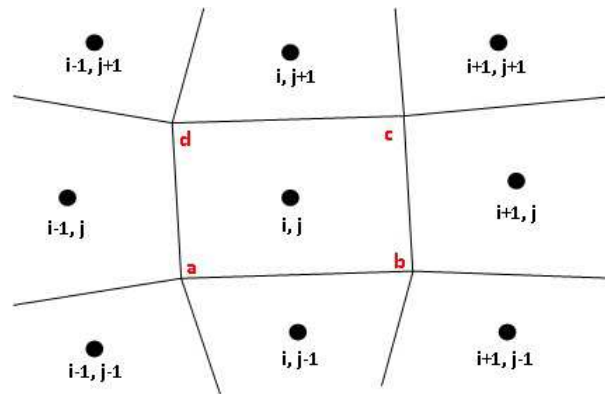


Figure 2: Quadrilateral control volumes and resulting structured grid.

Considering the Fig. 2, the first term of the left hand side of Eq. (2.5) (the unsteady term) is integrated over the control volume  $[i,j]$  as

$$\int_{abcd} \left( \frac{\partial f_\alpha}{\partial t} \right) dA \approx \left( \frac{\partial f_\alpha}{\partial t} \right)_{[i,j]} A_{[i,j]}, \quad (2.8)$$

where  $A_{i,j}$  is the area of the cell that is indexed as  $[i,j]$ .

For the integration of the second term of the left hand side of Eq. (2.5) (the advection term), the divergence theorem is applied;

$$\int_{abcd} (\vec{e}_\alpha \cdot \vec{\nabla} f_\alpha) dA = \oint_{abcd} (\vec{e}_\alpha \cdot \vec{n}) f_\alpha dl, \quad (2.9)$$

where  $\vec{n}$  is the unit normal vectors of the edges that form the cell considered. The right hand side of Eq. (2.9) can be separated into four parts for a quadrilateral cell as follows;

$$\begin{aligned} & \oint_{abcd} (\vec{e}_\alpha \cdot \vec{n}) f_\alpha dl \\ &= (\vec{e}_\alpha \cdot \vec{n}(ab)_{[i,j]}) f_\alpha(ab)_{[i,j]} l(ab)_{[i,j]} + (\vec{e}_\alpha \cdot \vec{n}(bc)_{[i,j]}) f_\alpha(bc)_{[i,j]} l(bc)_{[i,j]} \\ & \quad + (\vec{e}_\alpha \cdot \vec{n}(cd)_{[i,j]}) f_\alpha(cd)_{[i,j]} l(cd)_{[i,j]} + (\vec{e}_\alpha \cdot \vec{n}(da)_{[i,j]}) f_\alpha(da)_{[i,j]} l(da)_{[i,j]}. \end{aligned} \quad (2.10)$$

In Eq. (2.10),  $l$  terms are the length of each edge that forms the cell considered. For the evaluation of flux-terms introduced in Eq. (2.9), an interpolation scheme is needed to compute edge values of the distribution functions. For this purpose, the Monotone Upstream-centered Scheme for Conservation Laws (MUSCL) [15] might be used. For example, depending on the sign of the  $(\vec{e}_\alpha \cdot \vec{n}(bc)_{[i,j]})$  term, the distribution function on the  $bc$  edge is given as

$$f_\alpha(bc)_{[i,j]} = \begin{cases} f_\alpha_{[i,j]} + \frac{1}{4} \left( (1+\kappa) \cdot (f_\alpha_{[i+1,j]} - f_\alpha_{[i,j]}) + (1-\kappa) \cdot (f_\alpha_{[i,j]} - f_\alpha_{[i-1,j]}) \right) & \text{for } \vec{e}_\alpha \cdot \vec{n}(bc)_{[i,j]} \geq 0, \\ f_\alpha_{[i+1,j]} + \frac{1}{4} \left( (1+\kappa) \cdot (f_\alpha_{[i,j]} - f_\alpha_{[i+1,j]}) + (1-\kappa) \cdot (f_\alpha_{[i+1,j]} - f_\alpha_{[i+2,j]}) \right) & \text{for } \vec{e}_\alpha \cdot \vec{n}(bc)_{[i,j]} < 0, \end{cases} \quad (2.11)$$

where the term  $\kappa$  determines the spatial accuracy and by setting this term to  $1/3$ , one can obtain second order accuracy.

The term on the right hand side of Eq. (2.5) (the collision term) can be integrated using

$$-\frac{1}{\lambda} \int_{abcd} (f_\alpha - f_\alpha^{eq}) dA \approx -\frac{1}{\lambda} (f_\alpha - f_\alpha^{eq})_{[i,j]} A_{[i,j]}. \quad (2.12)$$

So, first, collecting the numerical flux terms together under

$$\begin{aligned} F_{[i,j]} &= (\vec{e}_\alpha \cdot \vec{n}(ab)_{[i,j]}) f_\alpha(ab)_{[i,j]} l(ab)_{[i,j]} + (\vec{e}_\alpha \cdot \vec{n}(bc)_{[i,j]}) f_\alpha(bc)_{[i,j]} l(bc)_{[i,j]} \\ & \quad + (\vec{e}_\alpha \cdot \vec{n}(cd)_{[i,j]}) f_\alpha(cd)_{[i,j]} l(cd)_{[i,j]} + (\vec{e}_\alpha \cdot \vec{n}(da)_{[i,j]}) f_\alpha(da)_{[i,j]} l(da)_{[i,j]}, \end{aligned} \quad (2.13)$$

the finite-volume formulation of the LBM for a sample cell of  $abcd$  as shown in Fig. 2 takes the final form given as

$$\left(\frac{\partial f_\alpha}{\partial t}\right)_{[i,j]} A_{[i,j]} + F_{[i,j]} = -\frac{1}{\lambda}(f_\alpha - f_\alpha^{eq})_{[i,j]} A_{[i,j]}. \quad (2.14)$$

## 2.4 Time advancement method

The previously mentioned works in the literature that adopt the finite-volume approach to use with the LBM rely on explicit schemes, such as forward Euler method used by Peng et al., Stiebler et al. and Patil et al. or explicit Runge-Kutta scheme used by Zarghami et al., to advance the solution in time. The advantage of the explicit schemes is that the implementation of these schemes is straightforward and the advancement in a time-level is fast. But, these schemes suffer from a strict stability condition. Since Eq. (2.5) is a hyperbolic equation with a stiff source term, the stability condition is even worse for this case. For better numerical stability, an implicit scheme should be used. On the other hand, implicit schemes require complicated implementation and the solution procedure is generally very expensive. The compromise between explicit and implicit schemes is the Implicit-Explicit Runge-Kutta (IMEX) scheme [16]. With this method, the governing equation is split into a non-stiff and a stiff component (convective and collision terms in Eq. (2.5) respectively). Then, an explicit scheme for the non-stiff part and an implicit scheme for the stiff part is applied. With this method, the computational effort is moderate compared to an implicit scheme while the stability bound is larger compared to an explicit scheme.

The IMEX scheme consists of multiple stages and the solution of each stage for the finite-volume based LBM, omitting the index  $[i, j]$  of control volume for convenience of writing, is given by the formula

$$f_\alpha^{(s)} = f_\alpha^n - \frac{\Delta t}{A} \sum_{k=1}^{s-1} \tilde{m}_{sk} F^{(k)} - \frac{\Delta t}{\lambda} \sum_{k=1}^s m_{sk} \left( f_\alpha^{(k)} - f_\alpha^{eq,(k)} \right), \quad (2.15)$$

where  $s$ ,  $f_\alpha^{(s)}$ ,  $f_\alpha^{eq,(s)}$ , and  $F^{(s)}$  are the stage number, the stage distribution functions, the stage equilibrium distribution functions, and the stage sum of numerical fluxes, respectively.  $f_\alpha^n$  represents the distribution functions of the time level. Then, the solution at next time level is given by

$$f_\alpha^{n+1} = f_\alpha^n - \frac{\Delta t}{A} \sum_{j=1}^r \tilde{n}_j F^{(j)} - \frac{\Delta t}{\lambda} \sum_{j=1}^r n_j \left( f_\alpha^{(j)} - f_\alpha^{eq,(j)} \right), \quad (2.16)$$

where  $r$  is the total number of stages. In addition, the  $r \times r$  matrices of  $\tilde{m}$  and  $m$  and the  $r$  vectors of  $\tilde{n}$  and  $n$  contain the coefficients that characterize the IMEX scheme.

The implicit part of the scheme, which is the last term on the right hand side of Eq. (2.15), includes two unknown from the stage that is being solved,  $f_\alpha^{(s)}$  and  $f_\alpha^{eq,(s)}$ . To fix these, the characteristic of the collision invariants of the LBM [17], that can be given as

$$\sum_{\alpha=1}^N \left( f_\alpha^{(l)} - f_\alpha^{eq,(l)} \right) \varphi = 0, \quad (2.17)$$

where  $N$  is the number of discrete velocity directions, is used to derive

$$\sum_{\alpha=1}^N (f_\alpha^{(s)}) \varphi = \sum_{\alpha=1}^N (f_\alpha^n) \varphi - \frac{\Delta t}{A} \sum_{k=1}^{s-1} \tilde{m}_{sk} \left( \sum_{\alpha=1}^N (F^{(k)}) \varphi \right) \quad (2.18)$$

from Eq. (2.15). In the above equations,  $\varphi$  is one the collision invariants of the LBM, i.e. 1 or  $\vec{e}_\alpha$ . From Eq. (2.18), the macroscopic variables of the stage being solved can be computed without knowing the stage distribution functions. With these, the stage equilibrium distribution functions can be found and rearranging Eq. (2.15) as

$$f_\alpha^{(s)} = \frac{f_\alpha^n - \frac{\Delta t}{A} \sum_{k=1}^{s-1} \tilde{m}_{sk} F^{(k)} - \frac{\Delta t}{\lambda} \sum_{k=1}^{s-1} m_{sk} (f_\alpha^{(k)} - f_\alpha^{eq,(k)}) + \frac{\Delta t}{\lambda} m_{ss} f_\alpha^{eq,(s)}}{1 + \frac{\Delta t}{\lambda} m_{ss}}, \quad (2.19)$$

stage distribution functions can be computed. Finally, using Eq. (2.16) the solution at next time step can be found. For the current implementation, a three stage IMEX scheme is used.

## 2.5 Boundary conditions

To implement the boundary conditions, the extrapolation method proposed by Guo and Zheng [18] is used. The main reason for choosing this method is that it provides a way of defining boundary conditions not in terms of distribution functions but in terms of macroscopic properties which are generally known. In addition, this method is shown to be of second order accurate by Guo and Zheng and exhibit better numerical stability than the alternative methods considered in the same reference for comparison purpose.

For the present implementation of the finite-volume based LBM, one level of ghost cells are defined on the borders of the solution domain and the appropriate macroscopic variables are set in those cells for a given boundary condition. The equilibrium distribution functions at the ghost cells are computed using the macroscopic variables. The distribution functions at the ghost cells are then found using

$$f_\alpha(\text{ghost cell}) = f_\alpha^{eq}(\text{ghost cell}) + [f_\alpha(\text{inside}) - f_\alpha^{eq}(\text{inside})]. \quad (2.20)$$

The second term of the right hand side of Eq. (2.20) means the non-equilibrium part of the distribution functions of the cell just next to the boundary.

## 2.6 Turbulence model

To model the effect of turbulence in the simulations, one-equation model of Spalart-Allmaras[19] is used. This turbulence model is based on the transport of an eddy-viscosity variable  $\tilde{v}$ . The transport equation for this model in non-dimensional form is given as

$$\frac{\partial \tilde{v}}{\partial t} = M(\tilde{v}) + P(\tilde{v}) - D(\tilde{v}), \quad (2.21)$$

where  $M(\tilde{v})$  is the combined advection/diffusion term and is given by

$$M(\tilde{v}) = -(\vec{u} \cdot \vec{\nabla})\tilde{v} + \frac{1+c_{b2}}{\sigma} \vec{\nabla} \cdot \left[ (v+\tilde{v}) \vec{\nabla} \tilde{v} \right] - \frac{c_{b2}}{\sigma} (v+\tilde{v}) \vec{\nabla}^2 \tilde{v}. \quad (2.22)$$

$P(\tilde{v})$  is the production term

$$P(\tilde{v}) = c_{b1}(1-f_{t2})\tilde{S}\tilde{v}, \quad (2.23)$$

$D(\tilde{v})$  is the destruction term

$$D(\tilde{v}) = \left[ c_{w1}f_w - \frac{c_{b1}}{\kappa^2}f_{t2}\left[\frac{\tilde{v}}{d}\right]^2 \right]. \quad (2.24)$$

The parameters that are used in the above equation of turbulence model are given as

$$\begin{aligned} \chi &= \frac{\tilde{v}}{v}, & S &= |\omega|, & f_w &= g \left( \frac{1+C_{w3}^6}{g^6+C_{w3}^6} \right), \\ f_{t2} &= C_{t3} \exp(-C_{t4}\chi^2), & f_{v2} &= 1 - \frac{\chi}{1+\chi f_{v1}}, & g &= r + C_{w2}(r^{6-r}), \\ \tilde{S} &= S + \frac{\tilde{v}}{\kappa^2 d^2 f_{v2}}, & f_{v1} &= \frac{\chi^3}{1+\chi^3 c_{v1}^3}, & r &= \frac{\tilde{v}}{\tilde{S} \kappa^2 d^2}, \end{aligned} \quad (2.25)$$

and  $c_{b1}$ ,  $c_{b2}$ ,  $\sigma$ ,  $\kappa$ ,  $c_{w1}$ ,  $c_{w2}$ ,  $c_{w3}$ ,  $c_{v1}$ ,  $c_{t3}$ , and  $c_{t4}$  are the model constants,  $\omega$  is the viscosity, and  $d$  is the distance to the closest wall boundary.

To solve the above given transport equation for the eddy-viscosity model, the same cell-centered finite-volume based approach is followed that is applied for the LBM before. This means that Eq. (2.21) is integrated for the eddy-viscosity variable over the same quadrilateral control volumes which are also used for the solution of the LBM. It must also be stated that the time advancement of the two solutions (i.e. distribution functions and eddy-viscosity variable) is segregated from each other, i.e. the eddy-viscosity variable of a time level is computed after the solution for the distribution functions is obtained.

The convection term of the turbulence model equation is calculated using first-order upwind scheme and the diffusion terms are discretized using second-order central difference scheme. The time advancement is done by the backward Euler scheme with an approximate factorization procedure. As for the boundary conditions, the eddy-viscosity

variable is set to zero at the wall boundaries and a ratio of laminar viscosity is used at the inflow boundaries. If there is an outflow boundary, the eddy-viscosity variable is extrapolated from the interior of the solution domain.

Once the eddy-viscosity variable is computed, the turbulent kinematic viscosity is found using the relation

$$v_t = f_{v1} \tilde{\nu}. \quad (2.26)$$

Finally, the relaxation time is updated with the total viscosity as

$$\lambda = \frac{\nu + v_t}{c_s^2}. \quad (2.27)$$

### 3 Validation of the method

To validate the method used in this study, various flow problems are solved. The first three problems are the laminar cases, namely flow inside a lid-driven cavity, over a flat plate, and a circular cylinder. Then, turbulent flow over a flat plate and a NACA 0012 airfoil is solved to show the validity of the turbulence model used.

#### 3.1 Laminar flow in a lid-driven cavity

Flow in a lid-driven cavity at four different Reynolds numbers that are ranging from 400 to 5000 is solved to observe the validity of the present method. At this range of Reynolds number, the flow inside the cavity might be considered as incompressible and laminar and the structure of the flow is characterized by a large vortex occupying almost the whole cavity. There are also two smaller vortices around the lower corners of the cavity and for higher Reynolds numbers (i.e. 3200 and 5000), a fourth vortex forms around the upper left corner. Once the converged solution is obtained, the results are compared with the well documented results of a high fidelity numerical study of Ghia et al. [20]. To make the comparison more realistic, a uniform grid of  $129 \times 129$  points for  $Re = 400, 1000,$  and  $3200$  and a  $257 \times 257$  grid for  $Re = 5000$  is used as Ghia et al. did.

The streamlines computed with the present method is shown in Fig. 3, and this figure reveals that the general flow structure is captured. For more detailed analysis, the horizontal and vertical velocity profiles along the geometric centerlines of the cavity are compared with the results obtained by Ghia et al. These comparisons are shown in Fig. 4. To show the capability of the present method, the results from a commercial, finite-volume based Navier-Stokes solver (i.e. FLUENT) with the same grids used is also added to the plots. As can be seen from these comparisons, an almost perfect match is obtained between the three methodologies.

Other than the validation purpose, this case is also used to investigate the numerical accuracy of the present method. For this purpose, two subsets of the uniform  $129 \times 129$  grid, that is used for the previous computations, is created. The resulting grids are also

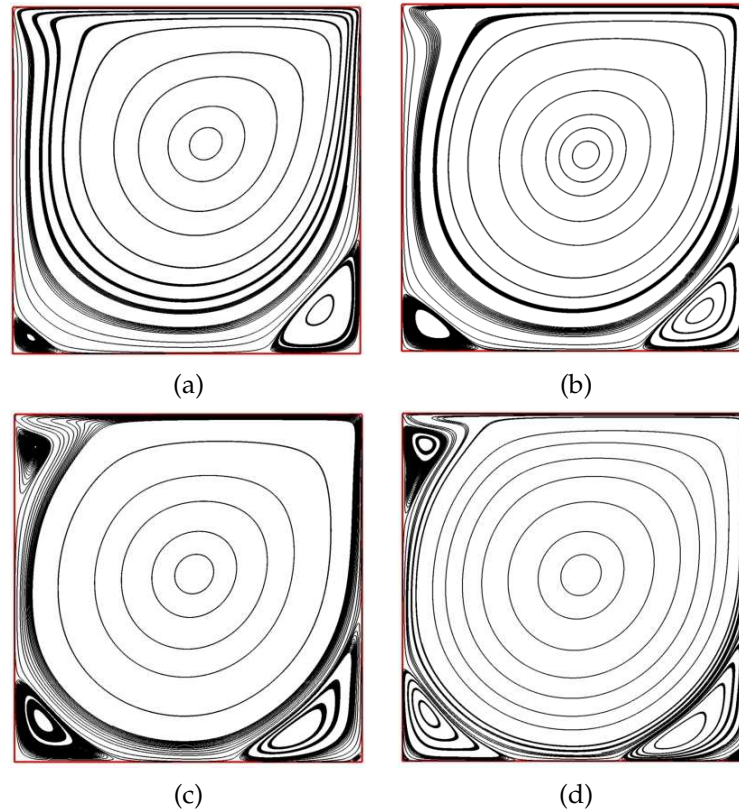


Figure 3: Streamlines computed inside the cavity with the present method for (a)  $Re=400$ , (b)  $Re=1000$ , (c)  $Re=3200$ , and (d)  $Re=5000$ .

uniform and consist of  $33 \times 33$  and  $65 \times 65$  points. Then, the numerical error on the horizontal velocity profile at  $Re=400$  with respect to the results of Ghia et al. is computed for each grid according to

$$\epsilon = \sqrt{\frac{\sum (u_{x,reference} - u_x)^2}{N^2}}, \quad (3.1)$$

where  $N$  is the spatial resolution in the grid (i.e. 33, 65, and 129). The resulting variation of the numerical error with the grid resolution along with  $-2$  slope is plotted in  $\log$  of the values and shown in Fig. 5. As can be observed from this figure, the present method has a spatial accuracy that is better than second order.

### 3.2 Laminar flow over a flat plate

Solution of the incompressible and laminar flow problem over a flat plate that is at zero angle of attack was first studied by Blasius [21]. The analytical solution proposed as a result of this study is now one of the best known validation cases used when validating

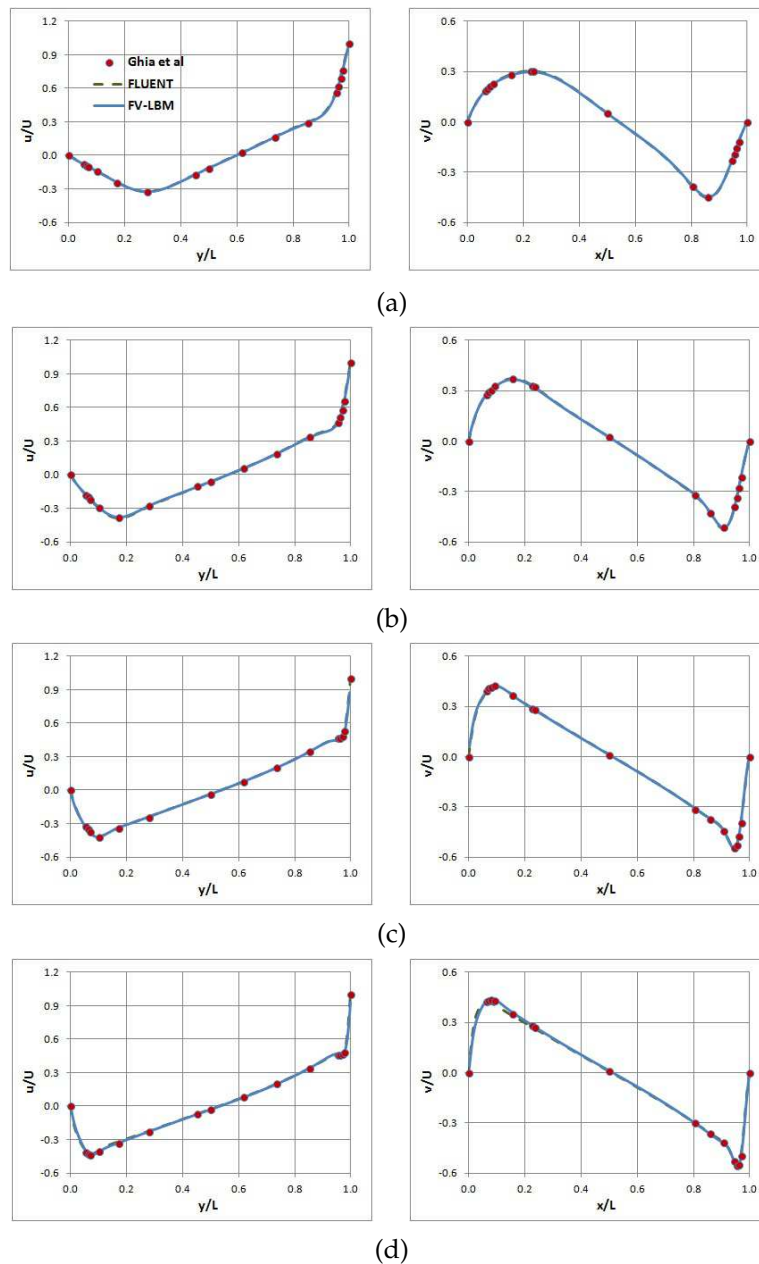


Figure 4: Horizontal (left side of the figure) and vertical velocity profiles along the geometrical centerlines of the cavity computed using FLUENT (dashed lines) and present method (solid lines) along with the results from Ghia et al. [20] (circles) for (a)  $Re=400$ , (b)  $Re=1000$ , (c)  $Re=3200$ , and (d)  $Re=5000$ .

flow solvers. To validate the present method solving this problem, two Reynolds numbers are considered, i.e. 10000 and 100000. A H-grid [22] that consists of  $273 \times 193$  points is generated to use in the simulations.

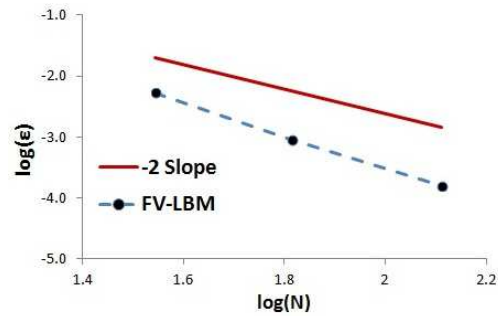


Figure 5: Variation of the numerical error with grid resolution for the lid-driven cavity flow at  $Re=400$ .

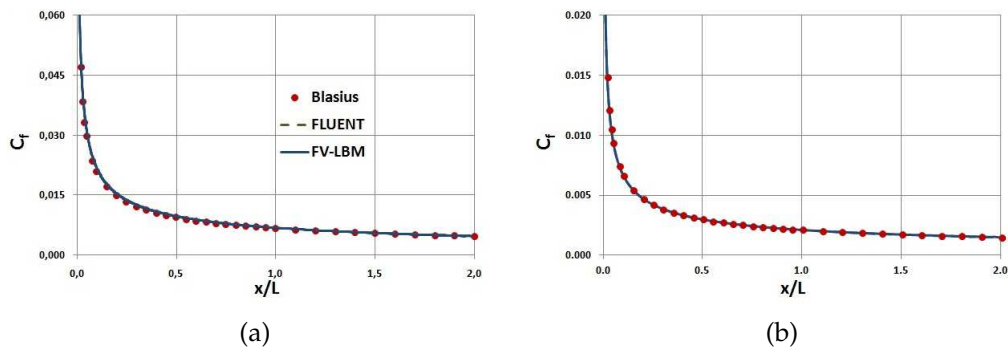


Figure 6: Skin friction coefficients over the flat plate computed using FLUENT (dashed lines) and present method (solid lines) along with the theoretical results of Blasius [21] (circles) for (a)  $Re=10000$  and (b)  $Re=100000$ .

The variation of the skin friction coefficients over the plate computed with the present method and FLUENT for  $Re=10000$  and  $100000$  are compared with the solution of Blasius and the results are shown in Fig. 6. As can be seen, very good agreement is obtained for both cases. Also, the non dimensional velocity profiles are compared and shown in Fig. 7. Here, the results obtained using the present method seems more satisfactory than FLUENT.

### 3.3 Laminar flow around a circular cylinder

The laminar and incompressible flow around a 2-D circular cylinder is solved to show how the present method can easily handle flow around curved boundaries as opposed to the standard LBM. For this case, three Reynolds numbers, which are equal to 10, 20, and 40, are considered. In these flow regimes, flow is separated and forms two counter-rotating vortices in the wake of the cylinder. For the simulations, an O-grid [22] of  $401 \times 201$  points is generated. Once the converged solutions are obtained, the length of the wakes, separation angles and drag coefficients are compared with the experimental and numerical data from the literature [23–26]. The computed streamlines are shown in

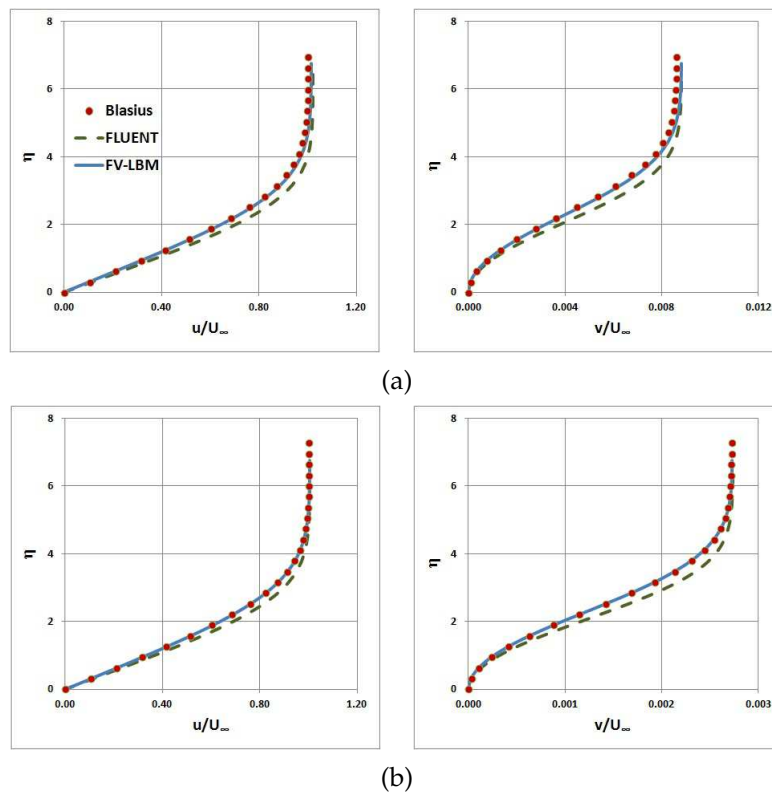


Figure 7: Non-dimensional horizontal (left side of the figure) and vertical velocity profiles computed using FLUENT (dashed lines) and present method (solid lines) along with the theoretical results of Blasius [21] (circles) for (a)  $Re=10000$  and (b)  $Re=100000$ .

Fig. 8. As can be observed from this figure, the expected counter-rotating vortices are captured for all the Reynolds numbers considered. The comparison of the wake lengths, separation angles, and drag coefficients with the data from the literature and the result from FLUENT is given in Table 2. A satisfactory agreement is obtained.

Table 2: Comparison of the wake lengths, separation angles, and drag coefficients for the cylinder.

	Re=10			Re=20			Re=40		
	L/r	$\theta$	Cd	L/r	$\theta$	Cd	L/r	$\theta$	Cd
[23]	0.434	27.96	2.828	1.786	43.37	2.053	4.357	53.34	1.550
[24]	0.680	32.50	-	1.860	44.80	-	4.260	53.50	-
[25]	0.474	26.89	3.170	1.842	42.90	2.152	4.490	52.84	1.499
[26]	0.498	30.00	-	1.804	42.10	-	4.380	50.12	-
FLUENT	0.468	28.79	2.769	1.802	43.38	2.006	4.460	53.64	1.500
Present Work	0.476	29.28	2.838	1.819	43.70	2.029	4.460	53.77	1.511

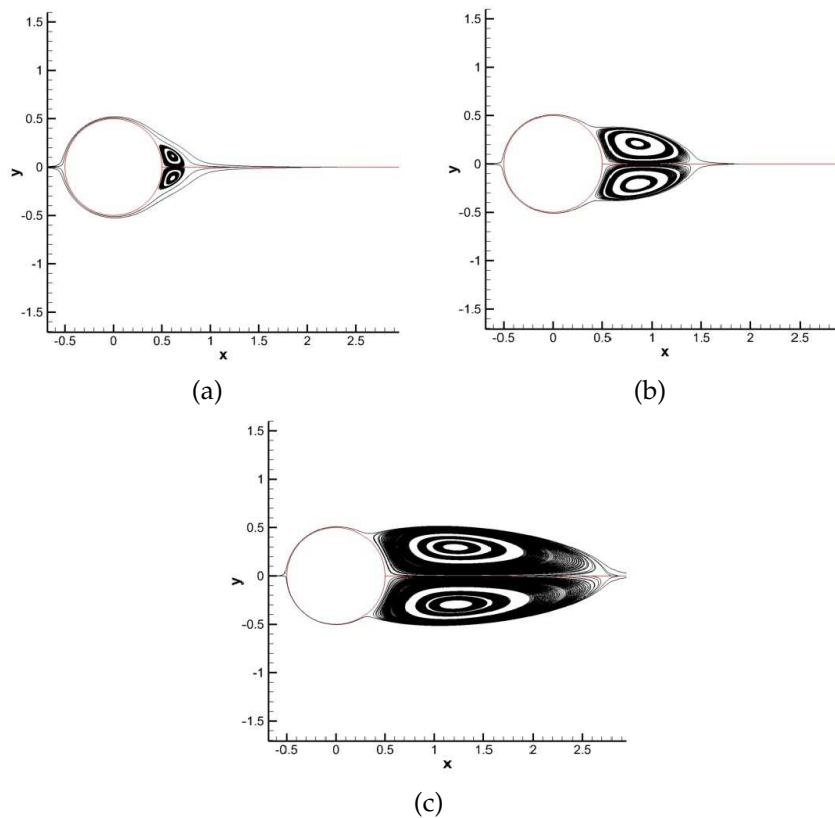


Figure 8: Computed streamlines around the cylinder for (a)  $Re=10$ , (b)  $Re=20$ , and (c)  $Re=40$ .

### 3.4 Turbulent flow over a flat plate

Since the method is validated against the laminar flow problems in the previous sections, the next task is to perform turbulent flow simulations. For this purpose, turbulent flow over a flat plate at zero angle of attack is considered first. An H-grid with  $545 \times 385$  points is used for this simulation. The Reynolds number considered is 5 million for unit length of the grid utilized. The reason for choosing this Reynolds number is the availability of simulation results that is given in by C. Rumsey in "SA Expected Results: 2D Zero Pressure Gradient Flat Plate through [http://turbmodels.larc.nasa.gov/flatplate\\_sa.html](http://turbmodels.larc.nasa.gov/flatplate_sa.html)" and obtained using a finite-volume based Navier-Stokes flow solver named as CFL3D with the same  $545 \times 385$  grid. The contour lines of the ratio of turbulent to laminar viscosity is given in the above mentioned reference, so, a comparison with the present simulation in this respect is possible and such a comparison is given in Fig. 9. As seen from this figure, almost the identical distribution of this value is captured with the present method compared with CFL3D code. The result from FLUENT differs in terms of maximum value from these two methods (see Fig. 9d), even though the same spatial discretization is used.

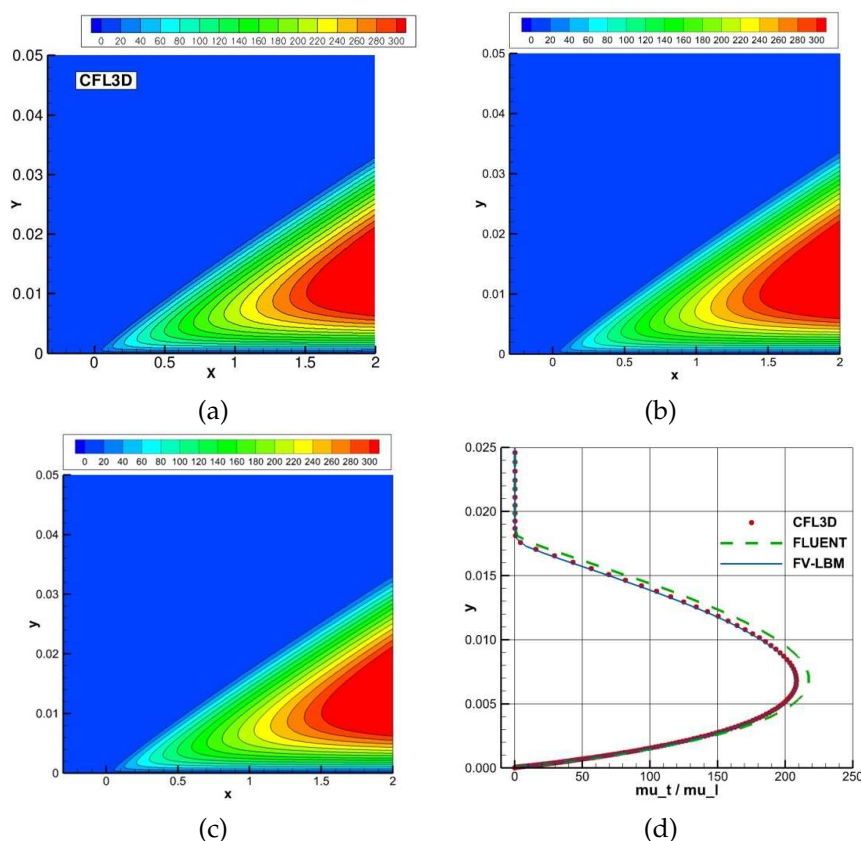


Figure 9: Contours of the ratio of turbulent to laminar viscosity over the flat plate computed with (a) CFL3D, (b) FLUENT, and (c) present method and (d) profile comparison of this ratio at  $x=0.97$  for CFL3D (circles), FLUENT (dashed line), and present method (solid line).

The computed skin friction coefficient is compared with the result from CFL3D code and also from FLUENT in Fig. 10. As can be seen, the skin friction coefficient computed by the present method matches very well with the result of CFL3D code as opposed to the result from FLUENT.

The horizontal velocity profiles at two different locations on the plate is also compared and shown in Fig. 11. All three flow solvers give almost identical results for this comparison.

### 3.5 Turbulent flow over a NACA 0012 airfoil

As the final case, turbulent flow over a NACA 0012 airfoil is considered to validate the present method. The flow conditions considered here correspond to a Reynolds number of 6 million. Various experimental data is available in the literature for this problem. Among them, the results obtained tripping the boundary layer are most appropriate,

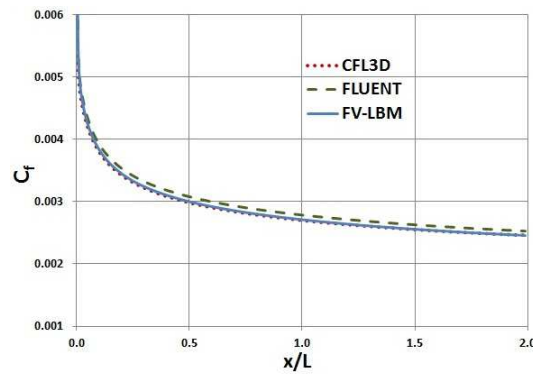


Figure 10: Comparison of skin friction coefficients over the flat plate for  $Re=5$  Million.

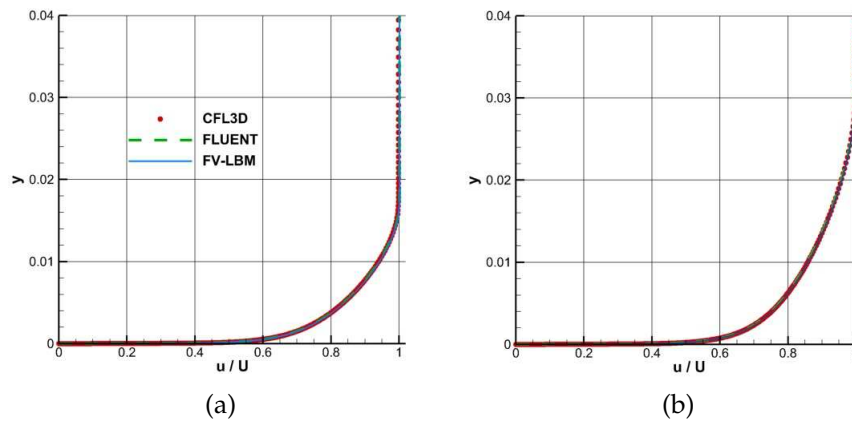


Figure 11: Horizontal velocity profiles over the flat plate computed using CFL3D (circles), FLUENT (dashed lines), and present method (solid lines) at (a)  $x=0.97$  and (b)  $x=1.90$ .

since the simulations performed for the current validation study are fully turbulent. So, for the comparison of computed and measured forces over the airfoil, data from Ladson [27] is used. On the other hand, since the resolution of the pressure data from other resources is not fine enough, results from the measurements of Gregory and O'Reilly [28] are used here for the comparison of upper surface pressure distributions. With a C-grid [22] of  $513 \times 257$  points used, distribution of pressure coefficient over the surface of the airfoil is computed for three different angle of attack values (i.e. 0, 10, and 15 degrees) and the results are shown in Fig. 12 along with the measured data of [28]. In this figure, the computed results present the distribution over the whole airfoil surface, so there are two distinct curves that correspond to the distribution over the upper and lower surfaces except for the 0 degree angle of attack case that has the single distribution since the airfoil is symmetric. Meanwhile, the experimental data is available only for the upper surface of the airfoil. As can be seen from the figure, the present finite-volume based LBM solver

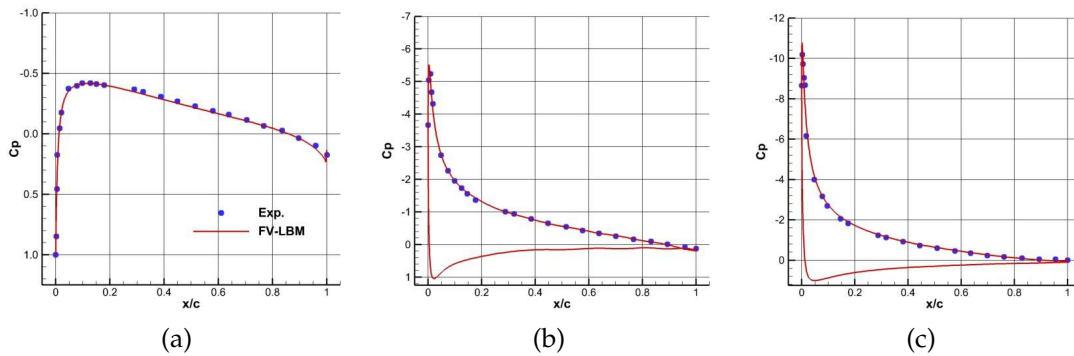


Figure 12: Upper surface pressure distributions over a NACA 0012 airfoil measured [28] (circles) and computed using present method (solid line) for angle of attack of (a) 0 deg., (b) 10 deg., and (c) 15 deg.

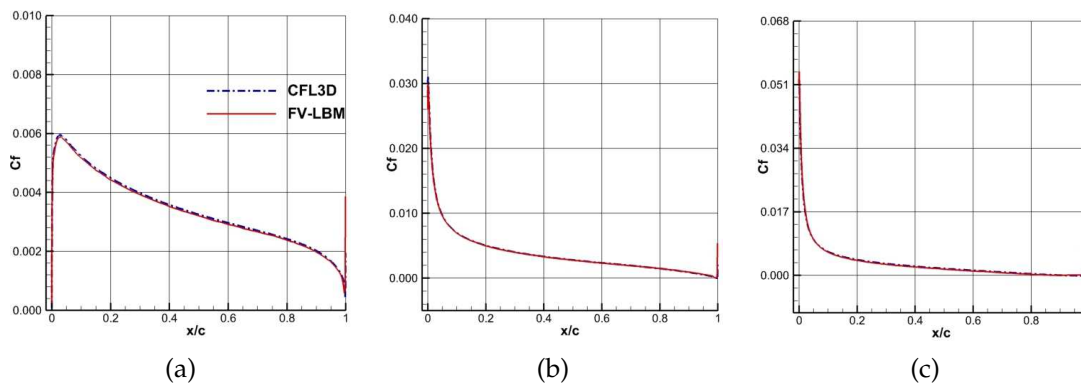


Figure 13: Upper surface skin-friction distributions over a NACA 0012 airfoil computed using CFL3D (dashed line) and present method (solid line) for angle of attack of (a) 0 deg., (b) 10 deg., and (c) 15 deg.

is sufficiently accurate, at least for the prediction of the pressure distribution over the airfoil's upper surface, since very good agreement is obtained between the experimental data and simulation results even though the flow considered here is attached for all three angle of attack values considered.

Furthermore, the computed skin-friction distribution over the upper surface of the airfoil using the present method is compared with the results from CFL3D code that is given by C. Rumsey in "SA Expected Results: 2D NACA 0012 Airfoil through [http://turbmodels.larc.nasa.gov/naca0012\\_val\\_sa](http://turbmodels.larc.nasa.gov/naca0012_val_sa)" and the comparison is given in Fig. 13. Again, very good agreement is obtained between the two methods in terms of the gradient of the velocity profile tangent to the wall.

Since both the pressure and skin-friction distributions over the airfoil surface is computed, it is also possible to compare the measured and computed forces on the airfoil, too. Such a comparison for all the angles of attack considered is given in Table 3. As can be seen, both the computed values with CFL3D (from the same website given in the previous paragraph) and the present method are very close to the measured ones.

Table 3: Measured and computed force coefficients for NACA 0012 airfoil.

	0 degree angle of attack		10 degrees angle of attack		15 degrees angle of attack	
	lift	drag	lift	drag	lift	drag
[27]	0.00000	0.00809	1.0586	0.01191	1.4961	0.01831
CFL3D	0.00000	0.00819	1.0909	0.01231	1.5461	0.02124
Present Work	0.00000	0.00818	1.0955	0.01236	1.5530	0.02143

## 4 Conclusion and future work

In this study, the LBM is implemented through a finite-volume approach to perform 2-D, incompressible, and turbulent fluid flow analyses on structured grids. Once validated solving various laminar flow problems, the one-equation turbulence model of Spalart and Allmaras is implemented into the solver. With available data from the literature, the turbulence model implemented is validated for the flow over a flat plate and a NACA 0012 airfoil. The obtained results show that the present method provides almost identical solution to the problems considered compared to the NS equations based flow solvers that are using the same spatial discretization schemes.

Since this study points that the present method is promising and can be an alternative to the NS equations based methods, a 3-D version of the flow solver might be implemented and more complicated flow problems can be studied. Furthermore, since the method is very suitable to be parallelized, a version of the solver that takes advantage of multi-threaded Graphics Processing Units (GPUs) might be implemented to obtain significant speed-up values.

## References

- [1] U. Frisch, B. Hasslacher and Y. Pomeau, Lattice-gas automata for the Navier-Stokes equation, *Phys. Rev. Lett.*, 56 (1986), 1505-1508.
- [2] G. Thömmes, J. Becker, M. Junk, A. Vaikuntam and D. Kehrwald, A Lattice Boltzmann Method for immiscible multiphase flow simulations using the level set method, *J. Comput. Phys.*, 228 (2009), 1139-1156.
- [3] X. M. Li, R. C. K. Leung and R. M. C. So, One-step aeroacoustics simulation using Lattice Boltzmann Method, *AIAA J.*, 44 (2006), 79-89.
- [4] S. Chen, A Large-Eddy based Lattice Boltzmann Model for turbulent flow simulation, *Appl. Math. Comput.*, 215 (2009), 591-598.
- [5] M. A. Fallah, V. M. Myles, T. Krüger, K. Sritharan, A. Wixforth, F. Varnik, S. W. Schneider and M. F. Schneider, Acoustic driven flow and Lattice Boltzmann Simulations to study cell adhesion in biofunctionalized  $\mu$ -fluidic channels with complex geometry, *Biomicrofluidics*, 4 (2010), 024106.
- [6] X. Y. He, L. S. Luo, and M. Dembo, Some progress in Lattice-Boltzmann Methods. Part 1. Nonuniform mesh grids, *J. Comput. Phys.*, 129 (1996), 357-363.

- [7] O. Filippova and D. Hanel, Boundary-fitting and local grid refinement for Lattice BGK Models, *Int. J. Mod. Phys. C*, 9 (1998), 1271-1279.
- [8] S. Succi, G. Amati and R. Benzi, Challenges in Lattice Boltzmann computing, *J. Stat. Phys.*, 81 (1995), 5-16.
- [9] P. L. Bhatnagar, E. P. Gross and M. Krook, A model for collision processes in gases, *Phys. Rev. Lett.*, 94 (1954), 511-525.
- [10] X. Y. He and L. S. Luo, Lattice Boltzmann Model for the incompressible Navier-Stokes equation, *J. Stat. Phys.*, 88 (1997), 927-944.
- [11] G. Peng, H. Xi, C. Duncan and S. H. Chou, Finite volume scheme for the Lattice Boltzmann Method on unstructured meshes, *Phys. Rev. E*, 59 (1999), 4675-4682.
- [12] M. Stiebler, J. Tolke and M. Krafczyk, An upwind scheme for the finite volume Lattice Boltzmann Method, *Comput. Fluids*, 35 (2006), 814-819.
- [13] D. V. Patil and K. N. Lakshmisha, Finite volume TVD formulation of Lattice Boltzmann simulation on unstructured mesh, *J. Comput. Phys.*, 228 (2009), 5262-5279.
- [14] A. Zarghami, M. J. Maghrebi, J. Ghasemi and S. Ubertini, Lattice Boltzmann finite volume formulation with improved stability, *Commun. Comput. Phys.*, 12 (2012), 42-64.
- [15] B. Van Leer, Towards the Ultimate Conservative Difference Scheme. V. A second order sequel to Godunov's method, *J. Comput. Phys.*, 32 (1979), 101-136.
- [16] S. Pareschi and G. Russo, Implicit-explicit Runge-Kutta schemes and applications to hyperbolic systems with relaxation, *J. Sci. Comput.*, 25 (2005), 129-155.
- [17] Y. Wang, Y. L. He, T. S. Zhao, G. H. Tang and W. Q. Tao, Implicit-explicit finite-difference Lattice-Boltzmann Method for compressible flows, *Int. J. Mod. Phys. C*, 18 (2007), 1961-1983.
- [18] Z. Guo, C. Zheng and B. Shi, An extrapolation method for boundary conditions in Lattice Boltzmann Method, *Phys. Fluids*, 14 (2002), 2007-2010.
- [19] P. R. Spalart and S. R. Allmaras, A one-equation turbulence model for aerodynamic flows, *AIAA Pap.*, AIAA-92-0439, 1992.
- [20] U. Ghia, K. N. Ghia and C. T. Shin, High-resolutions for incompressible flow using the Navier-Stokes Equations and a multigrid method, *J. Comput. Phys.*, 48 (1982), 387-411.
- [21] F. M. White, *Viscous Fluid Flow*, 2nd ed., Chap. 4, McGraw-Hill, 1991.
- [22] J. Blazek, *Computational Fluid Dynamics: Principles and Applications*, Chap. 11, Elsevier, 2001.
- [23] F. Nieuwstadt and H. B. Keller, Viscous flow past circular cylinders, *Comput. Fluids*, 1 (1973), 59-71.
- [24] M. Coutanceau and R. Bouard, Experimental determination of the main features of the viscous flow in the wake of a circular cylinder in uniform translation. Part 1: Steady flow, *J. Fluid Mech.*, 79 (1977), 231-256.
- [25] X. He and G. Doolen, Lattice Boltzmann Method on curvilinear coordinates system: Flow around a circular cylinder, *J. Comput. Phys.*, 134 (1997), 306-315.
- [26] R. W. Mei and W. Shyy, On the finite difference-based Lattice Boltzmann Method in curvilinear coordinates, *J. Comput. Phys.*, 143 (1998), 426-448.
- [27] C. L. Ladson, Effect of independent variation of Mach and Reynolds numbers on the low-speed aerodynamic of the NACA 0012 airfoil section, *NASA TM-4074*, 1988.
- [28] N. Gregory and C. L. O'Reilly, Low-speed aerodynamic characteristics of NACA 0012 airfoil section, including the effects of upper-surface roughness simulation hoar frost, *NASA RM-3726*, 1970.